Surface & Coatings Technology 494 (2024) 131325

Contents lists available at ScienceDirect

Surface & Coatings Technology

journal homepage: www.elsevier.com/locate/surfcoat

Anti-corrosion and anti-icing properties of superhydrophobic laser-textured aluminum surfaces

Peter Rodič [a], Nina Kovač [a,b], Slavko Kralj [c], Samo Jereb [d], Iztok Golobič [d], Matic Može [d,*], Ingrid Milošev [a]

[a] Jožef Stefan Institute, Department of Physical and Organic Chemistry, Jamova c. 39, SI-1000 Ljubljana, Slovenia
[b] Jožef Stefan International Postgraduate School, Jamova c. 39, SI-1000 Ljubljana, Slovenia
[c] Jožef Stefan Institute, Department for Materials Synthesis, Jamova c. 39, SI-1000 Ljubljana, Slovenia
[d] University of Ljubljana, Faculty of Mechanical Engineering, Aškerčeva c. 6, SI-1000 Ljubljana, Slovenia

ARTICLE INFO

Keywords:
Aluminum
Laser-texturing
Corrosion
Superhydrophobic surface
Anti-icing

ABSTRACT

Superhydrophobic surfaces have favorable properties in simultaneously reducing the negative effects of corrosion and ice accumulation. In this study, laser-texturing was employed as a facile and environmentally friendly surface method to prepare a surface with hierarchical roughness for subsequent grafting by immersion in an ethanol solution containing 1H,1H,2H,2H-perfluorodecyltriethoxysilane (FAS-10). Various analytical techniques were utilized to assess the characteristics of the laser-textured aluminum surfaces before and after grafting, such as a contact profilometer, optical tensiometer, scanning electron microscope with energy-dispersive spectroscope, and X-ray photoelectron spectroscope. These methods were used to evaluate surface roughness, wettability, morphology, and composition. The corrosion properties were evaluated through potentiodynamic and impedance measurements in a dilute Harrison's solution (DHS) composed of 0.35 wt% $(NH_4)_2SO_4$ + 0.05 wt% NaCl. Additionally, freezing delay tests at various surface temperatures were performed to assess the surface's ability to prevent the freezing of water droplets on the treated surface. The laser-textured aluminum surface, featuring micro/nanostructures and a grafted nanoscopic perfluoroalkyl silane film, exhibited outstanding superhydrophobicity and enhanced corrosion protection. The developed surface has been shown to significantly delay the onset of ice nucleation and extend the freezing delay.

1. Introduction

Low weight, high strength, and good corrosion resistance in atmospheric conditions are some of the main reasons for the extensive use of aluminum in construction and transportation industries and many other applications in everyday life [1]. The corrosion behavior of aluminum and its alloys depends on the corrosive medium, temperature, pH, and dissolved oxygen content. Major inorganic corrosive species in industrial and urban areas are ammonium (NH_4^+), sulfate (SO_4^{2-}) and nitrate (NO_3^-) ions found in the form of NH_4NO_3 and $(NH_4)_2SO_4$ (or NH_4HSO_4). These conditions can be simulated by the so-called dilute Harrison's solution (DHS) (0.35 wt% $(NH_4)_2SO_4$ + 0.05 wt% NaCl), which, in addition to Cl^-, also contains SO_4^{2-} and nitrate NO_3^- reflecting the environmental and atmospheric conditions [2]. Most corrosion studies are performed using NaCl solutions [1]; on the other hand, studies in the DHS are relatively rare.

Rapid developments have been made in superhydrophobic corrosion protective coatings in recent years [3,4]. These coatings also offer additional functional abilities of an aluminum surface once exposed to the real environment, including the adsorption of pollutants and ice formation [4–6]. Superhydrophobic surfaces have many uses because of their excellent properties, such as anti-icing [4,6–8], anti-fouling [9], and anti-bacterial applications [10]; therefore, there is a high potential for applications in different fields [4,5]. The definition of superhydrophobicity is based on the water contact angle of the droplet on the surface, which has to be larger than 150°, and a sliding angle smaller than 10° [11–13]. They can trap air in the modified surface topography, which prevents the aggressive ions from reaching the aluminum surface, consequently offering an efficient mechanism for corrosion protection [3–5,7,13,14]. Furthermore, reduced contact of water with the surfaces tends to notably delay the freezing of the said droplets on cold surfaces. The criteria for superhydrophobicity are not met naturally by untreated

* Corresponding author.
E-mail address: matic.moze@fs.uni-lj.si (M. Može).

https://doi.org/10.1016/j.surfcoat.2024.131325
Received 20 December 2023; Received in revised form 29 August 2024; Accepted 2 September 2024
Available online 10 September 2024

metallic surfaces, necessitating surface modifications to reduce their wettability. Although numerous studies related to superhydrophobic surfaces have reported their excellent performance in recent years, there is still a need to develop a convenient, environmentally acceptable, and facile method for fabricating superhydrophobic aluminum surfaces, capable of withstanding multiple adverse effects in a given application, such as corrosion and ice accumulation [5,13].

The wettability of a solid surface depends on surface roughness and surface chemistry [6,12]. There are several routes to construct superhydrophobic surfaces, such as the sol-gel process [15], anodic oxidation [16,17], chemical vapor deposition [18] and chemical etching [7,14,19–21]. However, once the practical application of such coating is considered, a method with simple operation, low cost and short operation time is required. From this point of view, laser-texturing to produce a roughened surface followed by grafting low-surface-energy organic materials such as fatty acids [19,20] or alkyl and perfluoroalkyl silanes [7,14,22] are one of the easiest, economical and environmentally acceptable routes [5,21]. Especially grafting of the aluminum surface with various alkyl and fluoroalkyl silanes (FAS) [7,23] have often been used due to the low surface energy of the CH, CF_2, CF_3 groups in the chain [7,24]. More specifically, FAS-10 consist of perfluorinated alkyl chain ($C_{10}H_4F_{17}$) attached to a silane group ($Si(OC_2H_5)_3$), which enables it to bond with various surfaces. [7] It is expected the monodentate and bidentate formation of the silanol monomer via the condensation mechanism on a hydroxylated aluminum substrate [25,26], forming a monolayer with the surface due to covalent bonding of the Al − O − Si. For instance, the treatment of aluminum or its alloys with fluoroalkyl silanes (FAS) in an alkaline solution has been utilized to prepare the superhydrophobic coating [7,27–30]. The initial silane precursors were hydrolyzed, condensed and covalently bonded on the activated aluminum surface, forming Al–O–Si bonds in an exothermic process [25,26]. Surface grafting reflects hydrophobicity, oleophobicity. Therefore such surface modification with desired properties finds applications in a wide range of industries, including electronics, optics, textiles, and coatings, where surfaces need to be rendered water and oil-repellent, anti-fouling, or easy to clean.

Superhydrophobic properties are the basis for several surface functionalities. In that context, the dynamic characterization of the water droplet on the surface [28] is essential to understanding the self-cleaning [14,31–33] and anti-icing properties [6,7,20,33,34]. For the latter application, minimized surface contact with a water droplet is desired to limit the heat transfer through reduced contact area and reduce the possible number of ice nucleation sites, generally provided through heterogeneous wetting in the Cassie-Baxter regime. [3] Furthermore, lower Gibbs free energy can make nucleation less thermodynamically favorable [6]. Finally, surface superhydrophobicity also aids anti-icing capabilities by possibly preventing prolonged contact between a droplet and the surface through water repellence and by facilitating easier ice removal through lower adhesion strength [6,8,33,34]. When water droplets fail to shed off the surface, it is favorable to both increase the required liquid supercooling before ice nucleation occurs and to increase the time delay until nucleation, which is followed by fast recalescence and much slower gradual solidification of the droplet [6,8].

In an effort to enhance anti-icing abilities of surfaces, many methods of surface functionalization to tailor their properties have been proposed. Guo et al. [8] combined micromachining, ZnO nanowire growth and fluorinated silane application on stainless steel, Sharafi et al. [35] proposed suspension plasma sprayed TiO_2 coatings, Liu et al. [36] treated aeronautical-grade steel with electrochemical etching and fluorosilane application, Bhushan and Her [37] used a two-step molding process and wax evaporation method to make superhydrophobic surfaces resembling artificial rose petals, Wang et al. [38] combined polydimethylsiloxane (PDMS) and ZnO nanohairs, Du et al. [39] used spray coating and a mixture of modified TiO_2 particles in polyaspartic acid ester polyurea to treat epoxy resin board, and Hou et al. [40] prepared anti-icing surfaces by constructing a series of micro-cubic arrays on silicon by selective plasma etching.

Within the context of surface functionalization for anti-icing applications, laser-texturing of the surface represents a flexible and quick method to impart micro- and nanostructures onto the surface through melting and ablation and thus provide the first step towards heterogeneous wettability. However, this needs to be supplemented by applying low-surface-energy materials onto the surface. The latter process can be natural (i.e., volatile organic compounds adsorption through prolonged exposure to ambient air), but to make the process repeatable and fast, various thin-film or thick coatings are more commonly used. To this effect, Lu [41] combined laser-texturing with micro milling, Li et al. [42] fabricated micron-structure gully and heatable hydrophobic graphene surfaces with direct laser writing on polyimide films, Xing et al. [43] used picosecond laser processing on 5052 aluminum alloy, Wang et al. [44] developed one-step laser surface texturing to fabricate robust superhydrophobic surfaces on stainless steel, Volpe et al. [45] impaired anti-icing properties on 2024 aluminum alloy with femtosecond laser-texturing and Zhan et al. [46] used a CO_2 laser to process polytetrafluorethylene (PTFE) directly. Despite several studies combining surface laser-texturing and hydrophobization to functionalize surfaces for anti-icing applications, there is still significant room for improvement in terms of using quick, scalable, flexible, and environmentally friendly methods to produce corrosion resistant surfaces with superior anti-icing capabilities.

In current work, superhydrophobic films on aluminum surfaces were fabricated using a two-step process consisting of selected laser surface texturing under optimal conditions to form a hierarchical micro−/nanostructure aluminum surface and controlled grafting in the ethanol solution of 1H, 1H, 2H, 2H-perfluorodecyltriethoxysilane (FAS-10) as a low-surface-energy material. The surface morphology and composition were studied to confirm the effect of laser-texturing and chemical bonding of FAS-10 on the surface. Additionally, the wettability, electrochemical, and anti-icing measurements were performed on the superhydrophobic film to understand better the functional properties, such as corrosion and anti-icing properties.

2. Material and methods

2.1. Metal substrates and chemicals

Aluminum 1050A H24 (Al > 99.5 %) in the form of a 5 mm thick sheet was distributed by MDM d.o.o. (Ljubljana, Slovenia). It was cut into plates sized 20 mm × 20 mm. The surface was sequentially ground in the presence of tap water with Struers LaboSystem LaboPol-20 machine using 1000 and 2000 SiC abrasive papers (supplied by Struers ApS, Ballerup, Denmark).

Laser-texturing was performed with a nanosecond pulsed fiber laser system (FL-mark C with JPT Opto-electronics “M7 30 W” MOPA source; wavelength of 1064 nm) in an ambient air atmosphere. A scanning speed of 500 mm/s, laser pulse frequency of 500 kHz, pulse length of 45 ns, and an average source power of 30 W were used. The diameter of the laser beam on the surface was approximately 25 μm, resulting in an average pulse fluence of 12.2 J/cm^2. A pattern of parallel lines with a spacing of 40 μm for the processing samples was used, as shown in Fig. 1.

Grafting was performed by immersion in 1 wt% 1H, 1H, 2H, 2H-perfluorodecyltriethoxysilane – FAS-10 ($C_{16}H_{19}F_{17}O_3Si$, > 97 %, CAS no. 101947–16-4, distributed by Sigma-Aldrich) ethanol solution (C_2H_5OH, absolute, anhydrous >99.9 %, CAS no. 64–17-5, distributed by Sigma-Aldrich) for 60 min as denoted in Fig. 1. This immersion time was chosen based on preliminary measurements [14,33]. The samples were positioned at the bottom of the beaker with the laser-treated surface facing up. Grafting was performed at room temperature. After each preparation step (grinding, laser-texturing, grafting), the samples were rinsed with distilled water and cleaned by immersion in pure ethanol in an ultrasonic bath to remove all grinding residuals, unreacted FAS-10

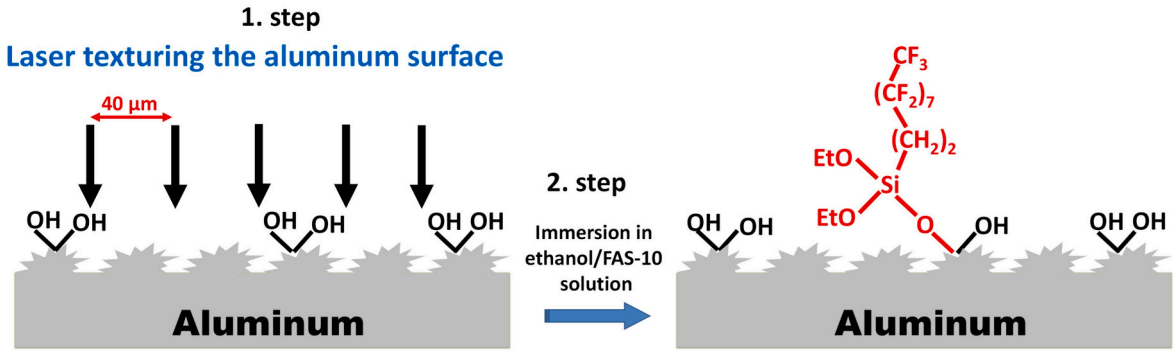

Fig. 1. Schematic illustration of forming a (super)hydrophobic aluminum surface prepared by the laser-texturing the surface with a pattern of parallel lines with a spacing of 40 µm followed by grafting with perfluoroalkyl silane, FAS-10.

and other organic substances present on the surface. Finally, the samples were dried with a stream of compressed air.

2.2. Surface characterization

2.2.1. Surface topography

Surface 3D topography and linear profiles of the laser-textured aluminum were evaluated on three randomly chosen spots, employing a stylus contact profilometer, model Bruker DektakXT, using a 2 µm diamond tip and in a soft-touch mode with force 1 mN. The measured surface was 1 mm × 1 mm, with a vertical analysis range of 65.5 µm using hills and valleys profile, a vertical resolution of 0.167 µm/point and map resolution of 10 µm/trace. Measured data were analyzed using TalyMap Gold 6.2 software. Results are presented as 3D images and line profiles, and their corresponding surface roughness (S_a) are given as mean values with error bars representing standard deviation.

2.2.2. Wettability

The wettability was characterized by two different solvents. The Milli-Q Direct water and diiodomethane (CH_2I_2, >99.0 %, CAS number: 75–11-6, distributed by Sigma-Aldrich) as two different polar solvents with the surface tension of 72.8 mN/m and 50.8 mN/m, respectively [7,47]. Contact angle measurements were performed at room temperature using the static sessile-drop method on a Krüss FM40 EasyDrop contact-angle measuring system. A small liquid droplet (4 µL) was formed on the end of the syringe, which was carefully deposited onto the treated aluminum surface. Digital image of the tested liquid droplet silhouette was captured with a high-resolution camera only a few seconds after droplet deposition on the surface to minimize the effect of solvent evaporation and changes in the drop shape. The contact angle was determined by fitting the droplet on the surface from the obtained image using associated protocol software for drop shape analysis. The values reported herein present the average of at least five measurements on five different droplets on various randomly chosen areas and are reported as mean values with error bars representing standard deviation.

2.2.3. SEM/EDS characterization

A scanning electron microscope (SEM) Thermo Fisher Verios 4G HP equipped with an energy-dispersive X-ray spectrometer (EDS) Oxford Instruments, AZtec Live, Ultim Max SDD 65 mm^2, Oxford Instruments, was used to analyze the morphology and composition of laser structured aluminum before and after grafting with FAS-10. The SEM imaging was performed using a secondary electron detector (SEI mode), and circular backscatter detector (CBS mode) of the specimens at 5 and 10 kV. The EDS analyses were performed on large selected area at 10 kV in area analysis mode to determine the average surface composition. The spot size of the electron beam at 10 kV is typically around 2–5 nm, offering good spatial resolution for imaging and analysis of samples in the SEM/EDS system. The data are given as an atomic percentage (at. %).

2.2.4. XPS characterization

The chemical compositions of laser-textured surfaces with and without the grafted FAS-10 were analyzed with X-ray photoelectron spectroscopy (XPS) using XPS spectrometer PHI TFA XPS, Physical Electronics USA, equipped with aluminum and magnesium monochromatized radiation. XPS survey and high-energy resolution spectra were collected using Al-K_α radiation (1486.92 eV). The pressure in the chamber was in the range of 10^{-9} mbar. A constant analyzer energy mode with 187.9 eV pass energy was used for survey spectra and 39.35 eV pass energy for high-energy resolution spectra. Photoelectrons were collected at a take-off angle 45° relative to the sample surface. The positions of all peaks were normalized concerning C 1 s peak at 284.8 eV. The elemental composition given as an atomic percentage (at. %) was determined from the survey XPS spectra using PHI MultiPak V8.0 software.

2.2.5. Corrosion properties

The corrosion testing was conducted in freshly prepared dilute Harrison's solution (DHS), which consisted of 0.35 wt% $(NH_4)_2SO_4$ (AppliChem ≥99 %) + 0.05 wt% NaCl (AppliChem >99.5 %) with pH 5.2. The solution was prepared in a volumetric flask using Milli-Q Direct water with a resistivity of 18.2 MΩ cm at 25 °C (Millipore, Billerica, MA).

Electrochemical measurements were performed at room temperature in a three-electrode corrosion cell (volume 250 mL). The working electrode was a ground, a laser textured, and a laser textured + FAS-10 grafted aluminum substrate with a 1.0 cm^2 surface exposed to the corrosive medium. A carbon rod served as a counter electrode. The reference electrode was saturated Ag/AgCl, (E = 0.197 V vs. standard hydrogen electrode).

Electrochemical tests were carried out with an Autolab PGSTAT 204 M (Metrohm Autolab, Utrecht, The Netherlands) potentiostat/galvanostat and controlled by Nova 2.1 software.

The samples were allowed to stabilize under open circuit conditions for 1 h. The stable, quasi-steady state potential reached at the end of the stabilization period is denoted as the open circuit potential (E_{oc}). Following stabilization, the electrochemical measurements were carried out. Potentiodynamic measurements were performed using a 2.2 mV step size and 1 mV/s potential scan rate, starting at −250 mV to E_{oc}. The potential was then increased in the anodic direction up to 0.6 V vs. Ag/AgCl. Measurements were performed at least in triplicate for each sample, and the representative measurement was chosen. Electrochemical corrosion parameters were obtained from polarization curves by Tafel approximation: corrosion current density (i_{corr}) and corrosion potential (E_{corr}). The pitting potential (E_{pit}) was determined as the potential in the passive region where the current density started to increase abruptly.

The corrosion behavior during long-term immersion was monitored using electrochemical impedance spectroscopy (EIS). The frequency range was from 100 kHz to 10 mHz at a sinusoidal voltage amplitude of 10 mV (rms). The measurements were performed with logarithmic frequency step type at 49 numbers of frequencies. The sample was immersed in DHS at ambient temperature up to 10 days. The EIS spectra were recorded at E_{oc} at selected time intervals. The Bode plots present the representative curves. The impedance values at 0.01 Hz are presented as average values of three measured samples (Bode plots are given in the supplement document as Figs. S1-S4).

2.2.6. *Anti-icing performance*

The anti-icing capabilities of the developed surfaces were evaluated by measuring the freezing delay. Water droplets were deposited onto the surface, which was then cooled to a desired temperature. Additional characterization was performed through high-speed video recordings of the recalescence phenomenon by tracking the freezing front travel versus time and by tracking the changes in droplet shape and volume during freezing.

To conduct the freezing delay measurements, a custom experimental setup was developed and utilized. The setup is shown schematically in Fig. 2a.

The setup was based around a closed, transparent chamber to conduct the experiments in a controlled humidity environment. The inner dimensions of the polymethymethacrylate (PMMA) chamber were 60 × 60 × 70 mm. To control the humidity, a custom loop desiccator was constructed by pumping the air in the chamber through a bed of silica gel beads before starting the measurement. During the measurement, the pump was turned off. A small container of silica gel beads was placed in the chamber when mounting the sample to provide additional dehumidification. Using this methodology, we were able to conduct all experiments at a relative humidity of 15–20 % at temperatures inside the chamber between 25 and 28 °C and at atmospheric pressure (~98–99 kPa). Cooling of the test surface was realized with a 2-stage thermoelectric (Peltier) cooler (AP2–162–1420-1118, European Thermodynamics) with an upper surface of 30 × 30 mm and maximal cooling capacity of 29.3 W and maximal temperature difference of 95 K. The hot side of the elements was cooled with a closed water-cooling loop. The sample was pressed onto the cooler with a 3D-printed polyethylene terephthalate glycol (PETG) holder, which limited heat exchange with the environment. Thermal paste was used to provide better thermal contact between the cooled and the sample. A K-type thermocouple was imbedded into the sample just below its surface to measure the surface temperature and provide a control input for the PID controller, which was used to power the thermoelectric cooler. A cross-section of the sample on the cooler is shown in Fig. 2b.

A Meerstetter TEC-1123-HV PID controller and the corresponding proprietary software were used to control the cooling process, stabilize the surface temperature and store the surface temperature readings. Additionally, a SparkFun RedBoard Qwiic was used to acquire data from auxiliary sensors in the system, including chamber temperature and humidity from a SparkFun Qwiic SHTC3 sensor and chamber pressure from the SparkFun Qwiic MicroPressure sensor. To deposit droplets of controlled sizes onto the sample, a microfluidic pump (NE-300) with a 5 mL glass syringe was used. Filtered twice-distilled water was pumped to a 34G needle integrated into the top cover of the experimental chamber. The droplet volume was measured to be approx. 3.7 μL with a corresponding equivalent diameter of 1.9 mm, comparable to typical droplet

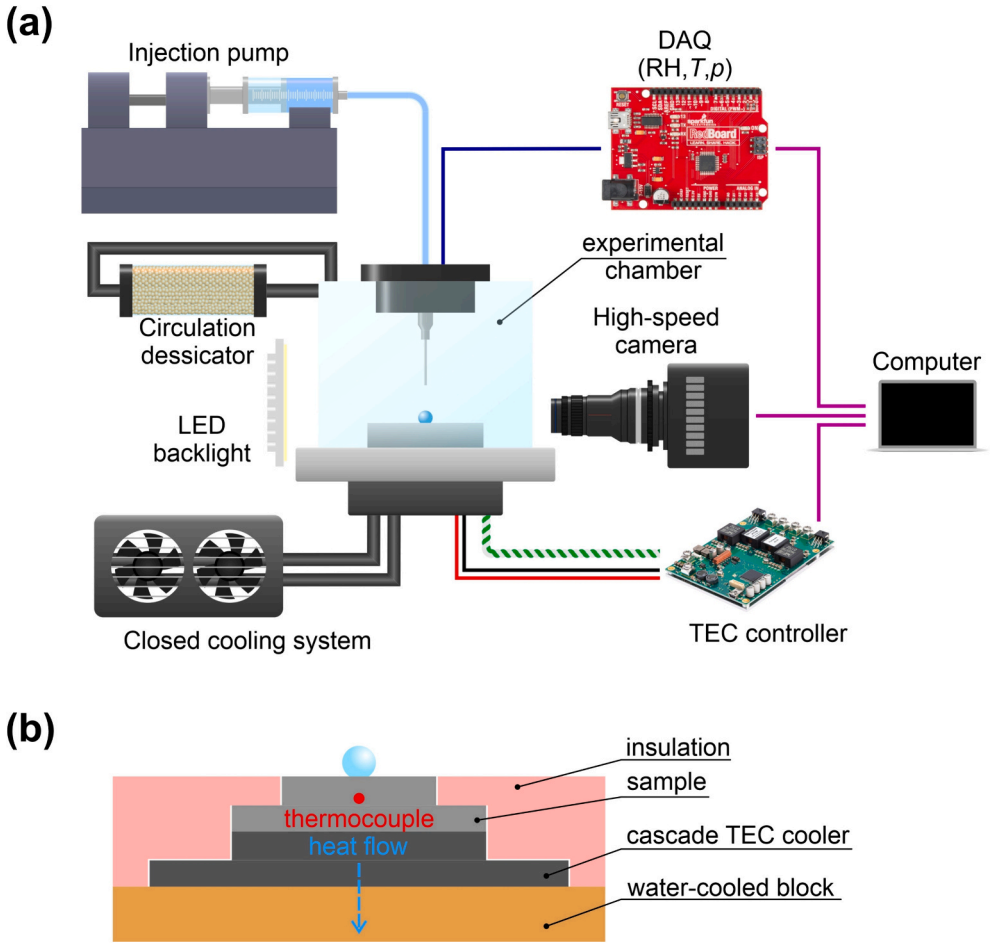

Fig. 2. Schematic illustration of (a) experimental setup for measuring freezing delay and (b) cross-section of the sample and the cooler.

volumes used in such experiments reported in the literature [48–51]. High-speed visualization of the freezing process was carried out with a Photron Mini UX100 camera at 500 frames per second using a Laowa 25 mm f/2.8 2.5-5× Ultra Macro lens. A high-power white LED backlight (Thorlabs SOLIS-2C) with a diffuser was used for illumination of the droplet. For general observations of the freezing delay, a monochrome USB camera (IDS UI-3060CP) with a macro lens, recording at 5 frames per second, was utilized.

The following experimental protocol was used to record the droplet freezing delay. The sample was mounted onto the cooling stage, and the chamber was closed. A droplet was deposited onto the surface using the syringe pump, and the desiccator was briefly running to reduce the humidity in the chamber. Then, the selected experimental temperature was set using the PID controller software, and the cooling process was started. When the water droplet started to freeze (i.e., at the start of ice nucleation), the freezing delay was recorded, and high-speed footage was saved. Measurements were repeated at least ten times at each temperature on every surface.

MathWorks MATLAB software was used to process the high-speed footage to determine the changes of droplet shape and volume during freezing. Initially, background subtraction was performed for each given frame, and afterwards, the droplet shape was detected using the Canny method. Assuming axial symmetry of the droplet, the volume was calculated based on the detected droplet edge.

3. Results and discussion

3.1. Bonding FAS-10 on a laser-textured aluminum surface

The two-step surface treatment to fabricate the superhydrophobic aluminum surface consists of laser-texturing of the aluminum surface to obtain a hierarchical micro−/nanostructure surface with a pattern of parallel lines with a spacing of 40 μm followed by grafting the surface in an ethanol solution of FAS-10 as a low-surface-energy material. According to the above description, the predicted reaction mechanism during surface treatment (laser-texturing + grafting) is schematically presented in Fig. 1.

The aluminum surface is affected during laser-texturing due to the progressive removal of the native passive film (Al_2O_3) and melting of the aluminum during laser ablation at selected areas [22]. After texturing, the aluminum sample reacts spontaneously with oxygen/humidity during rinsing with water which causes the passivation of the surface due to the formation of fresh aluminum oxide/hydroxide film containing OH^- groups (Fig. 1) [52]. In the second step denoted as grafting, reaction between hydroxylated Al and $(CH_3CH_2O)_3$–Si–$(CH_2)_2(CF_2)_7CF_3$ (FAS), where –OCH_2CH_3 (OEt-ethoxy group) presents a hydrolysable ethoxy group and –$(CH_2)_2(CF_2)_7CF_3$ a non-hydrolysable perfluoroalkyl chain, results in the formation of the surface film (Fig. 1). The chemical interfacial condensation and cross-linking reactions take place between the alkoxy and hydroxy groups of the laser-textured aluminum during the exothermic process [25,26], leading to robust covalent binding between the FAS molecule and aluminum surface according to Reaction 1:

$$Al\text{–}(OH)_3 + (CH_3CH_2O)_3\text{–}Si\text{–}(CH_2)_2(CF_2)_7CF_3 \rightarrow Al(OH)_2\text{–}O\text{–}Si\text{–}(OCH_2CH_3)_2\text{–}(CH_2)_2(CF_2)_7CF_3 + CH_3CH_2OH \quad (1)$$

The side product of this reaction is ethanol. As a result, the monodentate reaction between the surface and fluorosilane is expected (the condensation mechanism is exothermic by ≥0.5 eV) [22,25,26]. This process allows the integration of $(CH_2)_2(CF_2)_7CF_3$ functional groups on the aluminum surface. The perfluoro groups of the long perfluoroalkyl chain are oriented outward from the surface, creating a highly hydrophobic and oleophobic surface layer [20,53].

To sum up, the presence of Al–OH bonding on the freshly laser-textured aluminum surface is necessary to form a covalent bond between the aluminum surface and silicon, –Si–O–Al [25,26]. The results of the laser-texturing and grafting on the surface are discussed below.

3.1.1. Effect of surface treatment on topography

The surface roughness (S_a) of ground, laser-textured and laser-textured + FAS-10 is quantitatively presented in Fig. 3. The ground aluminum exhibits a smooth and flat appearance with small surface roughness, $S_a = 0.52 \pm 0.05$ μm. After laser-texturing, a significant transformation in the surface morphology of Al substrates becomes evident following the predefined laser scanning path.

The 3D surface profiles show that the dimensions of the roughness features for ground and laser-textured surfaces are at different scales and that the topography of the surfaces varies significantly with the laser-texturing (Fig. 3, left panel). During the laser treatment process, energy absorption and consequent removal of material create micro-scale patterns on the aluminum surface. Areas exposed to higher energy densities undergo melting and ablation [54]. Consequently, a grid-like pattern follows the predefined laser scanning path, giving rise to microstructures with hierarchical roughness with deposited materials in the interfacial regions. This process ultimately yields micro/nano hierarchical structures featuring microscale skeletal frameworks interlaced with redeposited nanoparticles. This surface texturing represents the initial stage in forming superhydrophobic surfaces, as it results in a micro−/nanostructure on the laser-textured Al surface, providing space for the presence of entrapped air [3,54]. The surface roughness of the laser-textured surface of the aluminum substrate increased by an order of magnitude to $S_a = 4.82 \pm 0.04$ μm. The increase in surface roughness correlates with that of laser processing; therefore, parameters can be well-controlled. After grafting with FAS-10, the surface roughness remained similar $S_a = 4.76 \pm 0.05$ μm, confirming that the formed FAS-10 film was a very thin monolayer and had a minor effect on surface roughness.

An increase in the number, size and depth of the holes in the laser-textured aluminum can be observed at line profiles (right panel). The line profile of the ground surface shows a random distribution of the bumps in the aluminum surface, with an average depth of 1 μm, probably related to the grinding process. A rough surface on the laser-textured surface with a variable number of valleys and hills was observed with an average depth of >8 μm. Moreover, line profiles show that the peak-to-peak and valley-to-valley distances align well with the applied laser-texturing parameters (line spacing of 40 μm).

A similar line macroscale roughness is also observed on the laser-textured+FAS-10 surface, Fig. 3. The increase in the number, size, and depth of the valleys at the laser-textured aluminum was not expected because only a monolayer of covalently bonded FAS-10 molecules on a laser-textured surface was formed. Therefore, the 3D or line profiles showed almost unchanged surface topography, Fig. 3.

3.2. Surface wettability

The surface wettability of ground, laser-textured and FAS-10-grafted aluminum was studied using polar solvent water (due to its bent shape and the difference in electronegativity between oxygen and hydrogen atoms in a water molecule), non-polar solvent diiodomethane (dipole

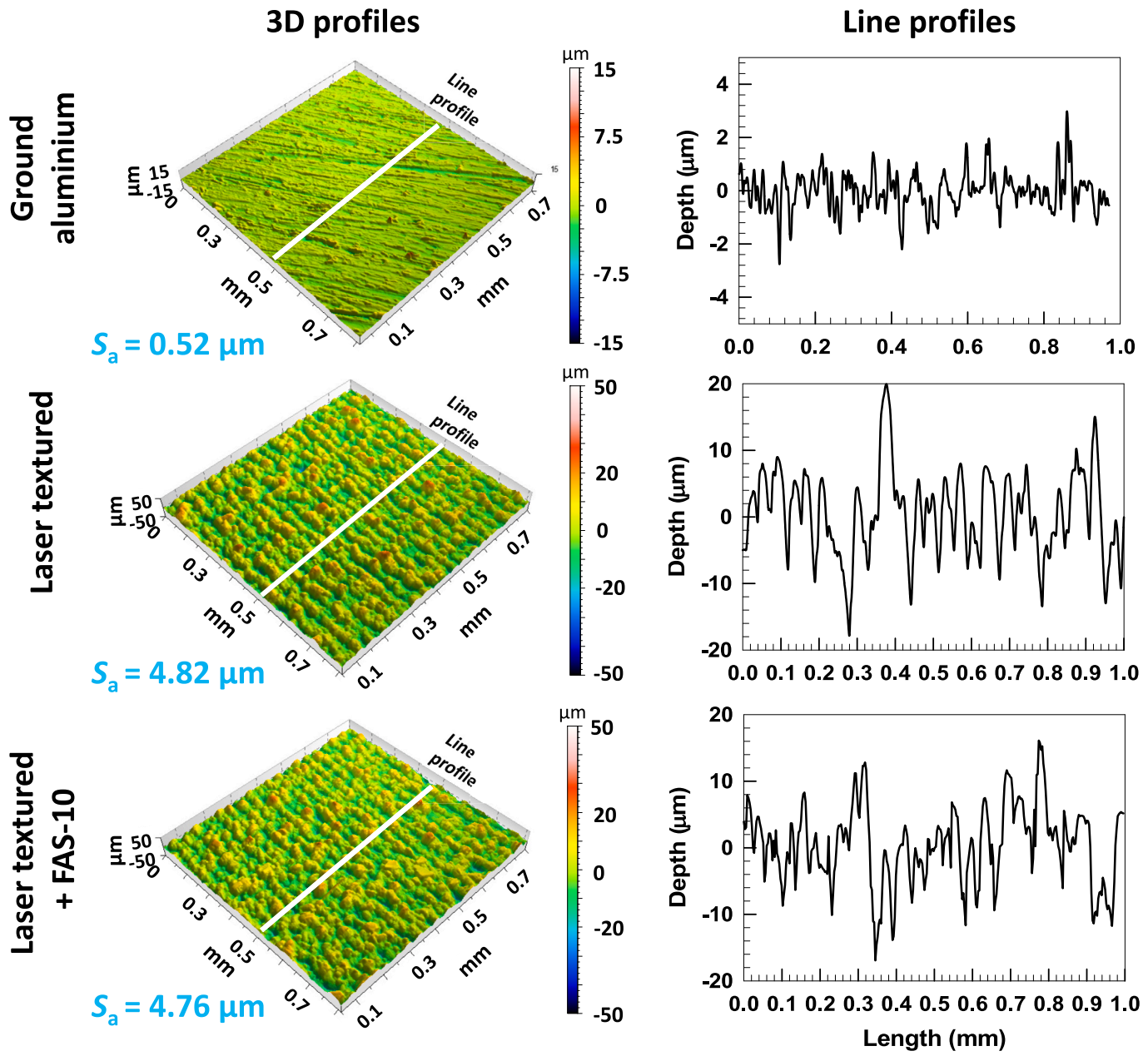

Fig. 3. (left panel) 3D surface topography images of the ground, laser-textured and laser-textured + FAS-10 grafted aluminum surface. The surface roughness values determined from 3D profiles are given in the figure. The white lines present an area where single-line profile analyses were performed (right panel).

moments of the two C—I bonds cancel each other out due to their symmetrical arrangement around the central carbon atom) (Fig. 4).

The non-ground aluminum surface is hydrophilic with a water contact angle (WCA) of about 45° due to the presence of a native oxidized layer spontaneously formed during extended exposure to air or moisture. The wettability of Al was enlarged by laser-texturing to produce a rough hydroxylated surface. Laser-textured aluminum is completely superhydrophilic, and WCA cannot be measured. Such behavior results from the presence of Al–OH groups formed during the laser-texturing [55].

The transition from a superhydrophilic surface, i.e., the laser-textured aluminum substrate, to a superhydrophobic surface occurred after grafting in FAS-10 solution. Based on previous results, it is known that the grafting of the as-received or ground aluminum substrate without laser-texturing was less efficient [14]. Since water is a polar molecule, it tends to exhibit stronger interactions with polar functional groups on a surface. On a superhydrophobic surface, water droplets will typically form a higher contact angle due to the minimization of the solid-liquid interaction energy. The water contact angle for laser-textured aluminum and FAS-10 grafted surface increased up to 155°, with the spherical shape of a water droplet on the surface, Fig. 4. This confirms that surface texturing is crucial to fabricating a superhydrophobic surface. In addition, the measurements were difficult to perform because if the surface was slightly tilted (<2°), water drops slid from the surface, confirming that treated aluminum has a low sliding angle. Two effects are interconnected: an increase in micro/nano roughness due to laser-texturing and the presence of low-surface-energy molecules (FAS-10) after grafting.

The static contact angles were also measured with less polar solvent diiodomethane, which strongly tends to interact with polar surfaces through dipole-dipole interactions or hydrogen bonding. On a superhydrophobic surface, the contact angle of diiodomethane was slightly

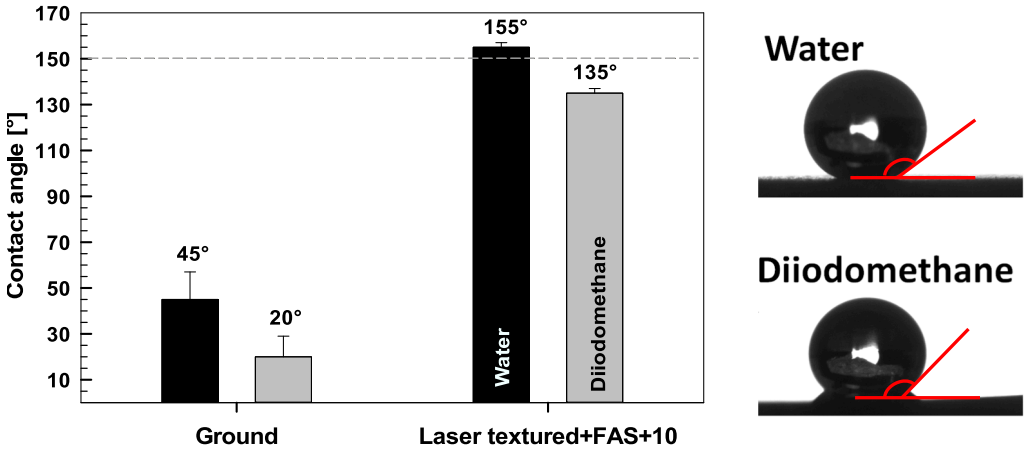

Fig. 4. Contact angles measured for water and diiodomethane at the ground and laser-textured aluminum surface and grafted for 1 h in 1 wt% ethanol FAS-10 solutions. The results are presented as mean values with error bars representing standard deviation. The dashed line presents the boundary of superhydrophobicity at 150°. The images of water and diiodomethane droplets on grafted aluminum with FAS-10 are also presented. The values for the laser-textured surface cannot be measured due to the superhydrophilic nature of the surface.

lower than that of water but still relatively high due to the minimization of solid-liquid interactions. CAs for diiodomethane increase with laser-texturing, but the maximum values are below 135°, reflecting hydrophobic surface with reduced spherical shape of a water droplet on the surface, Fig. 4.

From the obtained wettability data, it can be concluded that laser-texturing and grafting for 1 h in FAS-10 solution enables obtaining superhydrophobic properties with high water repellence (WCA above 150°, SA below 10°). Further characterization was carried out to determine the physico-chemical properties of the modified surfaces.

3.3. Composition, topography and morphology of aluminum grafted with FAS-10

3.3.1. SEM characterization of laser-textured and grafting aluminum surface

The topography and morphology of laser-textured aluminum were characterized using secondary electron (SE) mode (Fig. 5).

Laser-textured aluminum shows dispersed micro-scale holes with a width of <30 μm distributed throughout the surface (Fig. 5a,b). Also, nano-scale rectangular structures are distributed uniformly across the surface, making a hierarchical structure, Fig. 5b. The formed structures

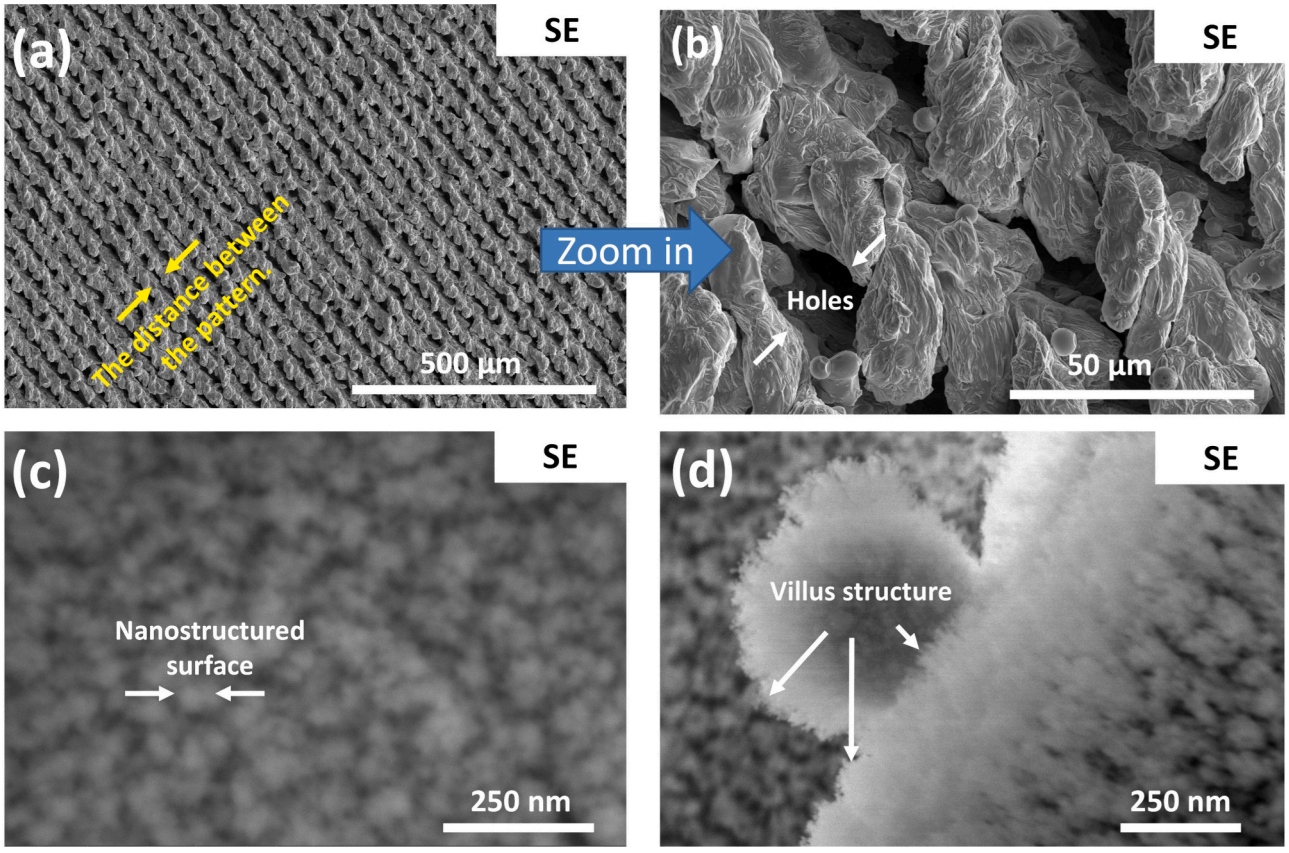

Fig. 5. SEM images of laser-textured aluminum recorded in SE mode at different magnifications.

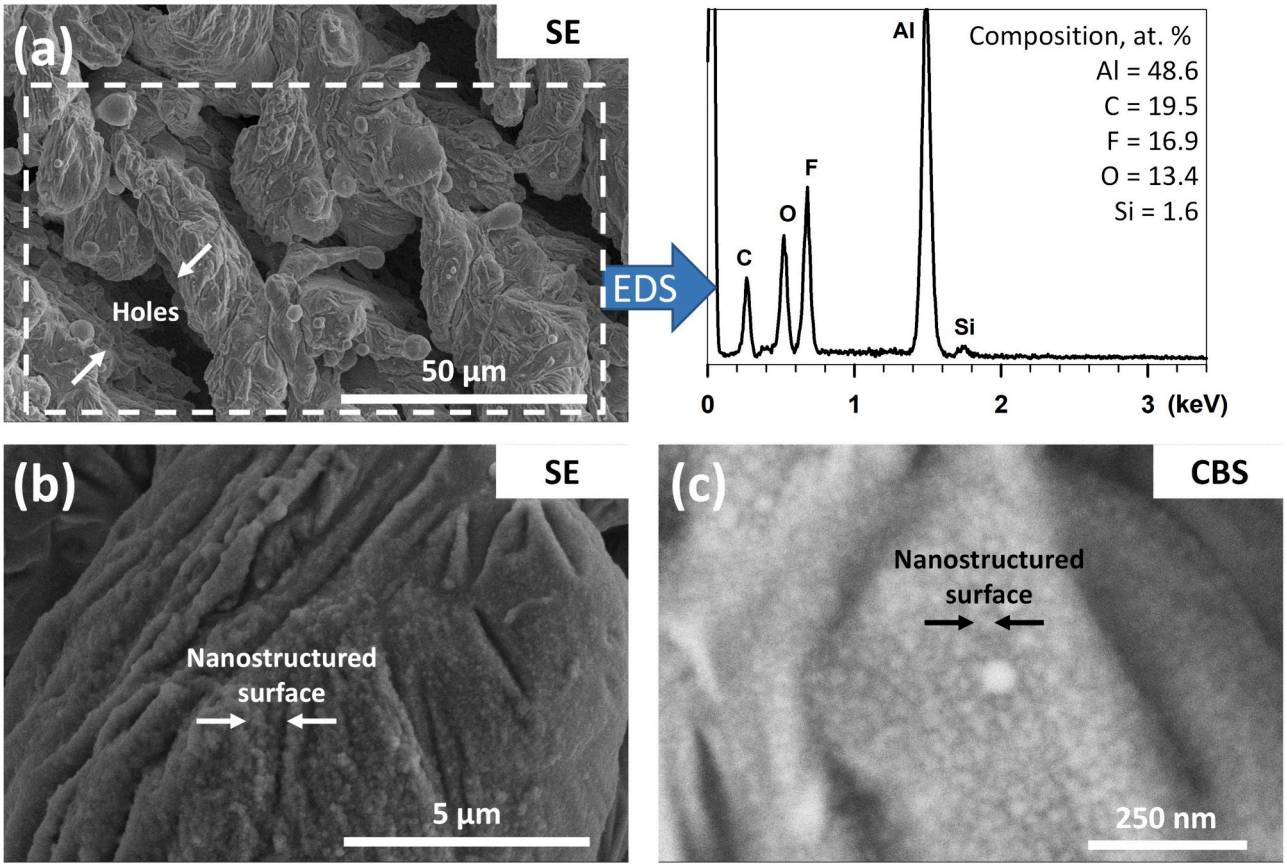

Fig. 6. SEM images recorded in SE and CBS mode of the laser-textured aluminum surface followed by grafting for 30 min in 1 wt% ethanol FAS-10 solution. The dashed square indicates an area where the EDS analysis was performed. The spectrum shows a representative composition in atomic percentage (at. %).

are of various dimensions; the estimated size is 30 µm; therefore, a binary structure of micro- and nanoscale is fabricated on the Al surface during laser-texturing, Fig. 5c. In addition, a nano-structured villus was formed, which enlarged the surface area and roughness, Fig. 5d.

Such a well-controlled laser-texturing process of the pattern of parallel lines was then further employed to fabricate a superhydrophobic surface on metal during grafting in an ethanol solution of FAS-10.

The topography and morphology of laser-textured aluminum were further characterized using secondary electron (SE) mode and circular backscatter detector (CBS) (Fig. 6).

The organic film formed by grafting is presumably nanometer-sized and thus cannot be easily analyzed by contact profilometry. Therefore, the surface morphology of the laser-textured and FAS-10-grafted surfaces was investigated by SEM/EDS. Fig. 6 shows the typical morphology of laser-textured aluminum grafted for 1 h using FAS-10.

After grafting, the changes between laser-textured surfaces without and with FAS-10 molecules are minor, Figs. 5b and 6a, but some changes in surface appearance can be noticed due to the formed film on the rough surface. Although the formed film was difficult to observe by SEM imaging recorded in SE mode, its presence was confirmed by comparing the chemical compositions of the laser-textured surface using the EDS (Fig. 6). The EDS spectrum of the sample surface demonstrates that the thin-formed film on the aluminum surface contains elements Al, F, C, O and Si. Al originating from the substrate predominates, while F and Si originate from FAS-10 molecules. The Si and F were detected in many analyzed areas on the aluminum matrix (data are not shown). The presence of these elements confirms the efficient grafting process and the formation of a monolayered film during immersion. At higher magnification, using the SE and CBS detectors, Fig. 6b,c, the micro-nano structured region (Fig. 6b) shows that the film evenly covers the surface. From the SEM imaging and surface analyses, it can be concluded that the combination of rough structures of the laser-textured aluminum surface and fluorinated functional groups in the FAS-10 molecule contributes to the superhydrophobicity of the sample surface [14,33].

3.3.2. *XPS analysis of laser-textured and grafting aluminum surface*

XPS analyses were performed to evaluate the chemical composition of laser-textured aluminum and grafting with FAS-10.

The survey XPS spectrum of laser-texturing aluminum is presented in Fig. 7a, where the identified elements originated from the substrate (Al), the passive film (Al and O), and the atmosphere (adventitious C) [52]. The chemical composition is given in Table 1.

The textured surface mainly consists of O and Al, which agrees with forming a spontaneously formed Al (hydr)oxide layer on a pure aluminum surface [14,52]. A small amount of adventitious C was detected. The survey XPS spectrum of grafted aluminum with FAS-10 strongly differs from laser-textured aluminum. The presence of Al, Si, F, C and O confirmed the grafting of FAS-10 film on the surface. F, C and O became the most abundant elements (Table 1). Al concentration decreases after grafting due to the formed film covering the textured aluminum surface [14]. However, it is still detected, indicating that the grafting monolayer of FAS-10 on a laser-textured aluminum surface is thinner than 10 nm, which is the depth of XPS analysis. The thickness of the formed monolayer can not be determined with XPS more precisely due to the rough laser-textured aluminum surface [56].

The aluminum surface was additionally analyzed with high-energy resolution XPS spectra (Fig. 7b-f). Al 2p and O 1 s spectra of laser-textured aluminum confirmed the presence of aluminum oxide/hydroxide (Fig. 7b,c). According to the XPS database [52,57,58], spectra related to the presence of AlOOH (74.7 eV, 531.7 eV) and passivation during exposure to air Al_2O_3 (73.1 eV, 530.7 eV) [52]. The carbon is present as adventitious carbon with a single sharp peak at 284.8 eV

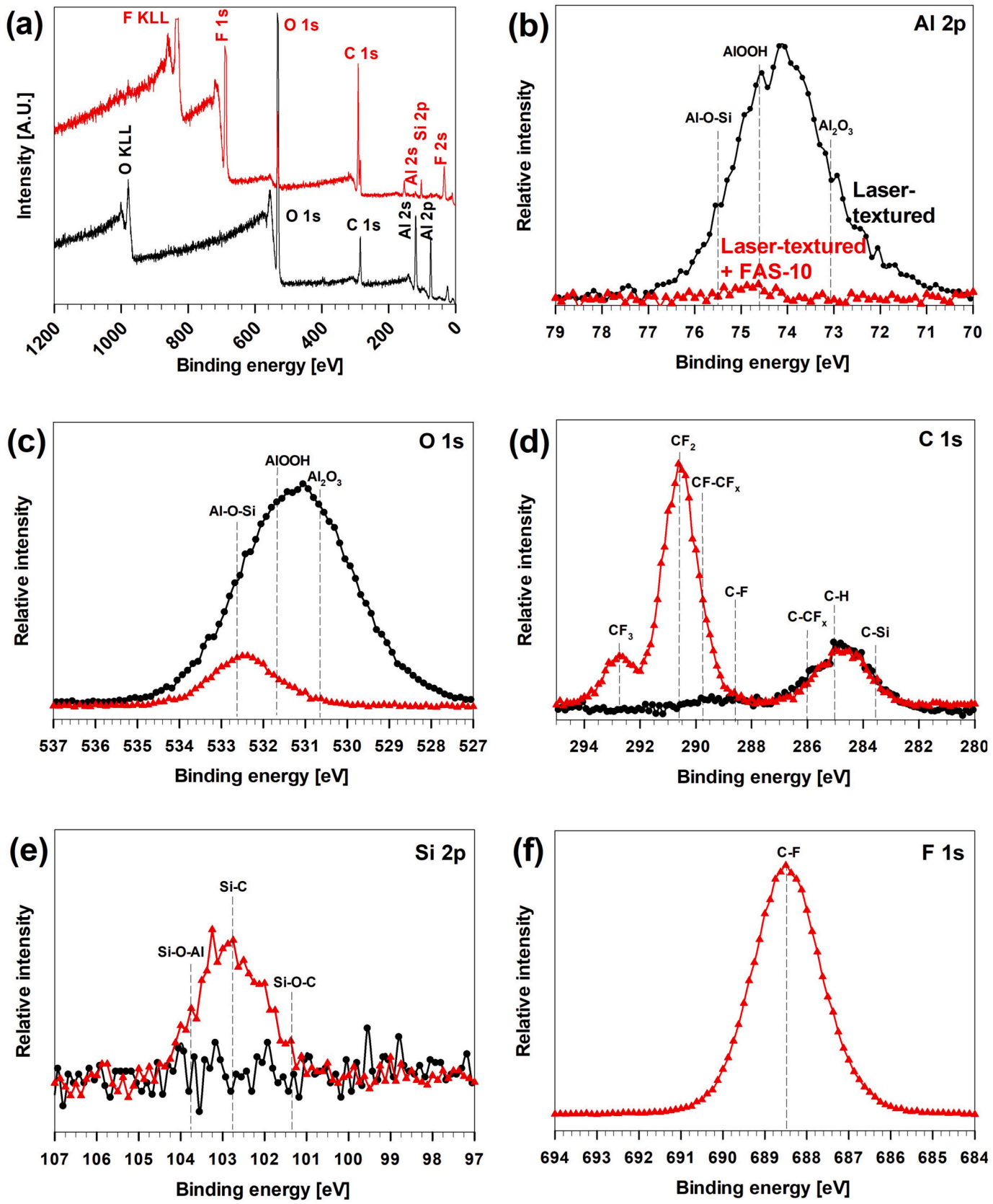

Fig. 7. (a) XPS survey spectra and high-energy resolution XPS of (b) Al 2p, (c) O 1 s, (d) C 1 s, (e) Si 2p and (f) F 1 s: symbols and solid lines present experimental spectra, vertical dashed lines present the position of component peaks. Spectra were recorded for laser-textured aluminum (black dots) and laser-textured aluminum grafted for 1 h in 1 wt% ethanol FAS-10 solution (red triangles).

Table 1
Composition determined by XPS analysis in at.% for laser-texturing aluminum and laser-texturing aluminum FAS-10 grafted surface (Fig. 7a).

	Aluminum textured surface	Aluminum textured surface + FAS-10
Al	29.9	0.9
O	55.6	6.5
C	14.5	33.1
Si	0	3.1
F	0	56.4

(Fig. 7c). The presence of OH is essential for efficient grafting of the surface [14].

On the other hand, grafted aluminum shows the broadening of the peaks Al 2p and O 1 s due to the presence of the third component related to Al–O–Si (at 75.5 eV and 532.7 eV, respectively) formed during grafting in FAS-10 solution. Therefore, the XPS data confirmed the formation of a monolayer covalently bonded on Al surface [25,26], formed between Al–OH + $(CH_3CH_2O)_3$–Si–$(CH_2)_2(CF_2)_7CF_3$ as presented by reaction 1. This is further corroborated by the C 1 s spectrum (Fig. 7d). The peak can be resolved into seven components, namely –CF_3 (294.0 eV), –CF_2 (291.8 eV), –CF–CF_x (290.8 eV), C—F (289.8 eV), –C–CF_x (286.7 eV), –C–C (284.8 eV) and –C–Si (283.8 eV). The characteristic bands of the fluoroalkyl groups (CF_2, and CF_3) confirmed the bonded FAS-10 molecules at the surface [59,60]. The intensity of CF_2 peak is equal to C—C and higher to CF_3 peak because the FAS-10 contains more CF_2 groups than CF_3 and C—C bonds. The Si 2p peaks comprised three components (Fig. 7e) with binding energy at about 101.3 eV for Si–O–C, 102.5 eV for Si—C associated with the FAS molecule [57,58] and at 103.7 eV associated with the Si–O–Al species formed during grafting [57,58].

The presence of the FAS-10 molecule can also be confirmed in F 1 s spectra, where a broad peak between 686 and 691 eV is related to the C—F covalent bond in the FAS-10 molecule (Fig. 7f). The CF_3 and CF_2 concentrations present in the C 1 s spectrum of the FAS-10-treated Al are in correlation with the molecular structure. The high concentration of CF_3 and CF_2 on the surface indicates that molecules are orientated with the Si—O bond to the surface, forming Si–O–Al, while $(CH_2)_2(CF_2)_7CF_3$ tail comprises the outermost surface film. Such surface composition correlates with the obtained reduced wettability [30,33].

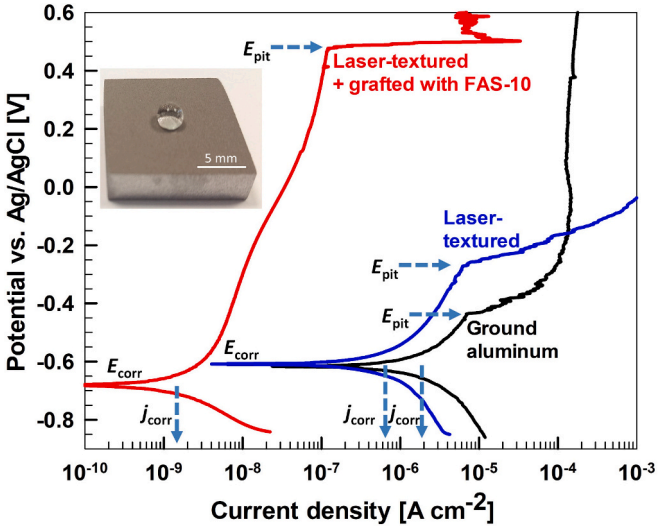

Fig. 8. Potentiodynamic polarization curves for laser-textured and grafted aluminum treated with fluoroalkyl silanes measured in dilute Harrison's solution (DHS) after immersion for one hour. dE/dt = 1 mV/s. The insert image shows the water droplet on LT + FAS-10 treated surface.

Table 2
Evaluated electrochemical parameters measured in dilute Harrison's solution for ground, laser textured and laser-textured+grafted with FAS-10: corrosion potential (E_{corr}), corrosion current density (j_{corr}), and pitting potential (E_{pit}) were determined from potentiodynamic polarization curves ($\Delta E = |E_{pit} - E_{corr}|$) in Fig. 8.

	E_{corr} [V]	j_{corr} [nA/cm^2]	E_{pit} [V]	ΔE [mV]
Ground aluminum	−0.62 ± 0.02	1540 ± 30	−0.44 ± 0.01	180
Laser-textured	−0.61 ± 0.03	411 ± 5	−0.26 ± 0.03	350
Laser-textured + grafted with FAS-10	−0.68 ± 0.03	0.9 ± 0.05	0.47 ± 0.05	1150

3.4. Corrosion properties

The corrosion performances of non-hydrophobized (i.e., only ground and laser-textured) and FAS-10-treated aluminum were characterized by utilizing electrochemical measurements (Fig. 8, Table 2).

The ground aluminum surface exhibits current density (i_{corr} = 1540 nA/cm^2), negative corrosion potential (E_{corr}) of −0.62 V and pitting potential (E_{pit}) at −0.44 V, $\Delta E = (E_{pit} - E_{corr})$ is 180 mV, Table 2. After the laser-texturing, the corrosion performance is affected by the changes in the morphology and composition of the surface hydroxylated film, Figs. 3, 7, [61,62]. The i_{corr} was reduced to 411 nA/cm^2, E_{corr} slightly shifted to less negative to −0.61 V and E_{pit} at −0.26 V (ΔE = 350 mV). These changes are due to the formation of a more dense and stable passive film on the aluminum surface under intense laser treatment compared to ground surface [63].

Fig. 8 shows the potentiodynamic curves for aluminum treated with fluoroalkyl silanes. The corrosion resistance of aluminum was effectively enhanced by grafting the surface with silane molecules. The E_{corr} was slightly negatively shifted to −0.68 V and j_{corr} was reduced to 0.9 nA/cm^2, Table 2. Especially due to reduced j_{corr}, the tendency of the treated aluminum to corrode was remarkably lower. Moreover, the E_{pit} was shifted to a high positive value (0.47 V), and ΔE extended to over 1.15 V for FAS-10, confirming that the formed monolayer protected aluminum against localized corrosion, even better than chemically-etched and FAS-grafted surface assessed under comparable testing conditions [7,14].

A correlation exists between the WCAs and corrosion resistance. j_{corr} decreased and ΔE extended as the aluminum surface became superhydrophobic, i.e., at a WCA = 155°. The formed film leads to a more compact structure, which acts as a more efficient corrosion barrier, preventing further corrosion of the aluminum substrate [13]. Superhydrophobic surfaces are characterized by their extremely low affinity for water, which causes water droplets to bead up and roll off the surface easily, thus reducing the contact area between the surface and corrosive agents [3,13]. This behavior is probably related to the strong molecular interactions (hydrogen bonds between C − F and Al − OH), which also affected the coating formation and its structure. Compared to data for other anticorrosion and superhydrophobic Al-based surfaces, the laser-textured and FAS-treated Al shows superior performance with a decrease in j_{corr} for more than two orders of magnitude compared to non-treated Al [64] because formed monolayer acts as an additional protection against corrosion, that reducing the corrosion current density. The results are comparable to those of thicker sol-gel coatings in the micrometer range [65]. Such corrosion performance may be due to a synergy of the barrier property of the adsorbed organic molecules and trapped air in the micro−/nanostructure of the surface; their combination prevents the transport of ions such as SO_4^{2-} and Cl^- ions in the corrosive medium through the surface layer from reaching the surface of aluminum. Due to the capillary effect, the corrosive medium is pushed out from the porous structure and bands up to a ball shape on the superhydrophobic surface [66].

In the next step, the Bode curves measured by EIS were studied as an

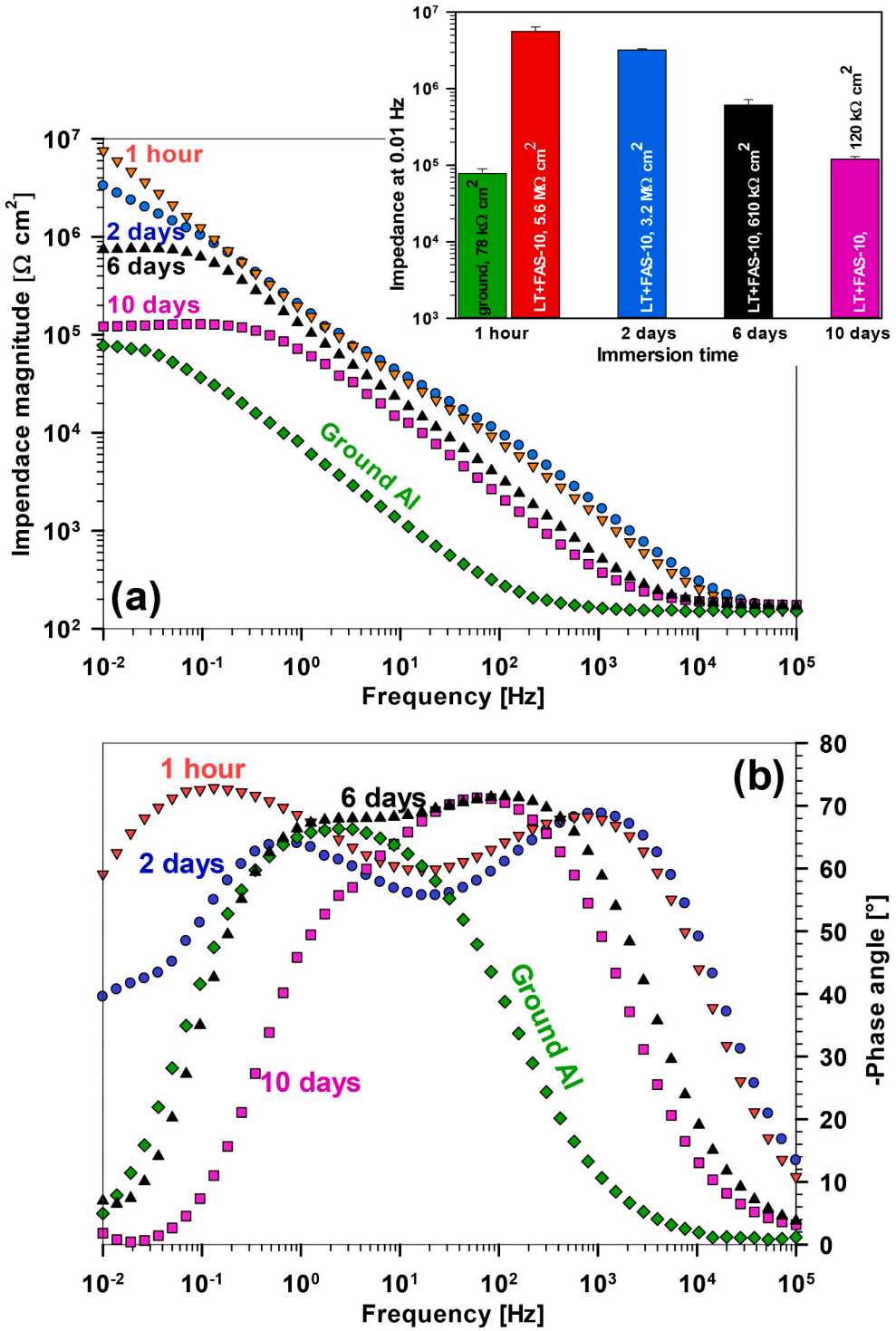

Fig. 9. Bode plots of (a) impedance magnitude with the inserted figure of average impedance values at 10 mHz (Fig. S1-S4) and (b) phase angle of laser-textured + FAS-10 grafted surface measured after various immersion times in dilute Harrison's solution (DHS) solution. The measurement for ground aluminum after 1 h of immersion is added as a reference.

effective tool for investigating the corrosion behavior of prepared samples and their durability. In Fig. 9, Bode impedance magnitude and phase angle with the maximum at the middle frequencies depict the corrosion performance of ground and laser-textured+FAS-10 aluminum samples immersed in a dilute Harrison's solution for 1 h. From Bode impedance magnitude, the corrosion resistance of samples can be compared by accounting for the impedance at low frequency (0.01 Hz), denoted as $|Z|_{0.01\ Hz}$. Higher $|Z|_{0.01\ Hz}$ indicates superior corrosion protection performance, insert figure in Fig. 9, supplement Figs. S1-S4.

The ground and samples exhibit typical impedance behavior of naturally passivated aluminum surface, with $|Z|_{0.01\ Hz} = 78 \times 10^3\ \Omega.cm^2$ [67,68]. Due to the low stability of the passive film in the tested solution, the maximum phase angle was 66°, Fig. 9b.

On the other hand, the Bode plot showed that the laser-textured+FAS-10 sample had enhanced anticorrosion properties, Fig. 9, Figs. S1-S4. The $|Z|_{0.01\ Hz}$ increased to the average value of $5.6 \times 10^6\ \Omega$.

cm^2, and the phase angle plot reveals two maximums, where the high-frequency loop signifies the barrier effect of the formed protective film, and the low-frequency indicates the electrochemical interaction of film with the substrate. The effects of laser-texturing followed by FAS grafting on the EIS spectra are greater than other pre-treatments, such as chemically etched or laser-etched superhydrophobic coating [7,14,22].

A long-term immersion test (up to 10 days in DHS) was conducted for the laser-textured+FAS-10 grafted sample (Fig. 9, Figs. S1-S4). The $|Z|_{0.01\ Hz}$ values remained high even after the extended immersion period. Coating provides a continuous barrier layer, acting as an effective insulator against the corrosive environment, resulting in a prolonged anticorrosion performance (after 2 days $|Z|_{0.01\ Hz} = 3.2 \times 10^6\ \Omega.cm^2$ and after 6 days $|Z|_{0.01\ Hz} = 6.1 \times 10^5\ \Omega.cm^2$). This confirmed the enduring corrosion protection ability of FAS-10 coating. The enhanced corrosion resistance of superhydrophobic samples compared to ground aluminum is attributed to their exceptional anti-wetting properties, the presence of an air cushion under water droplets, and the reduction of the contact area with the corrosive environment even after 6 days of immersion [3,14]. The reduction of the phase angle values at low frequencies was noticed, and after 6 days, the two maximums in the phase angle were merged into one, Fig. 9b, Fig. S3. Such behavior is related to the transition between different wetting states (e.g., Cassie-Baxter to Wenzel state) and reveals insights into the slowly decreasing of the system stability [13]. The changes reflect increased interactions between the corrosion medium and the aluminum surface.

However, this air cushion are displaced over time and corrosion media wets the surface. After 10 days, the corrosion performance was reduced due to local corrosion starts at some areas. [22,67] $|Z|_{0.01\ Hz}$ and phase angle became similar to that of ground Al that was tested after 1 h of immersion ($|Z|_{0.01\ Hz} = 1.2 \times 10^5\ \Omega.cm^2$), because the corrosion process degradants the formed nanoscopic perfluoroalkyl silane film.

3.5. Anti-icing performance

Freezing delay measurements using water droplets of a constant size were conducted at different surface temperatures both on an untreated reference surface and the superhydrophobic laser-textured surface to evaluate the anti-icing abilities. Since significant droplet spreading and low contact angles were observed on laser-textured surfaces without the hydrophobic coating, no freezing experiments were conducted on them as such wetting behavior decreases the freezing delay and is thus unfavorable for most applications.

Fig. 10 compares the freezing delay on the reference untreated surface and the laser-textured FAS-10 grafted surface at −10 °C, −15 °C and − 20 °C. The superhydrophobic surface managed to significantly delay the freezing of a water droplet at every temperature. The significance of the increased freezing delay was confirmed by one-way ANOVA and post-hoc Tukey HSD test, with the calculated *p*-values at all temperatures falling well below the 0.05 significance threshold. Notable standard deviations, as evident in Fig. 10, are common in freezing delay investigations due to the inherent stochastic nature of the nucleation phenomenon responsible for the liquid-solid phase change [69]. For this reason, as explained before, all experiments were repeated multiple times. The scatter of the data was further analyzed by conducting 30 independent measurements on the FAS-10 surface at −20 °C, where we observed a mean delay of 61.3 s, a median of 49.0 s, and a standard deviation of 25.2 s.

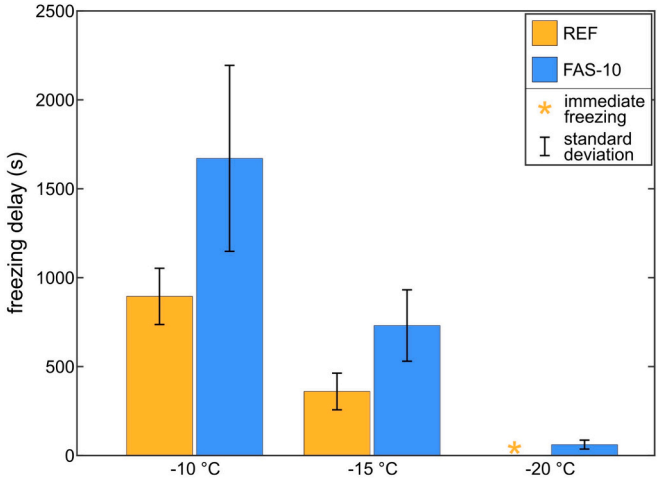

Fig. 10. Freezing delay at three surface temperatures for the untreated surface (REF) and the superhydrophobic laser-textured surface (FAS-10).

Further analyses were performed using high-speed footage to compare the freezing process on the untreated and the superhydrophobic FAS-10 surfaces. Fig. 11a compares droplet height and volume change during freezing on the reference and FAS-10 surfaces. On both samples, freezing was initiated by droplet recalescence, turning subcooled liquid into a mixture of water and ice crystals, causing the droplet to expand in a matter of a few milliseconds. In Fig. 11a, the rapid expansion of droplets appears as an instantaneous increase in droplet volume and height at the beginning of the freezing process. Recalescence was followed by isothermal freezing, during which a freezing front appeared at the droplet-solid interface and gradually moved upwards to the top of the droplet, turning the remaining liquid into ice and thus making the droplet completely solid. Liquid-solid phase change during isothermal freezing caused the droplet to increase in volume and height further. The increase of height with time was relatively linear for the untreated as well as the superhydrophobic surface in the first half of the isothermal freezing; however, in the second half, the rate of growth

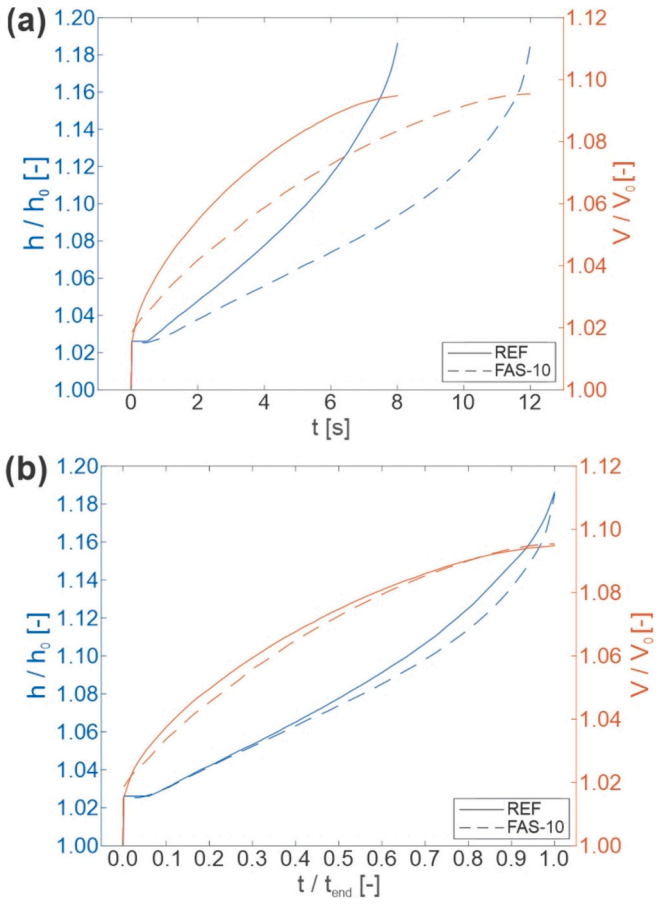

Fig. 11. Droplet volume and height change during the freezing process on reference untreated surface and FAS-10 surface with (a) absolute time scale and (b) normalized time scale.

increased due to the formation of a peak at the top of the droplet [70]. On the contrary, the rate of droplet volume change decreased with time due to the growth of the frozen layer retarding the heat transfer between the remaining liquid and the surface [71–73]. Total expansion of the droplet was independent of surface treatment as the droplet volume and height increase was roughly 10 % and 20 %, respectively, compared with the initial value for both substrates. However, superhydrophobicity significantly impacted the time needed for the freezing front to reach the top of the droplet, as it was 50 % longer on the FAS-10 surface than the untreated surface. This can mainly be attributed to the smaller contact area between the solid and the droplet on the superhydrophobic surface and the presence of entrapped air beneath the droplet, increasing the thermal resistivity and thus reducing the heat flow rate [74]. Normalization of the time axis shown in Fig. 11b allows a more detailed comparison of droplet freezing kinetics on the reference and the superhydrophobic surface. There was a noticeable difference in the period of the constant increase rate of droplet height between the samples, which was longer on the FAS-10 surface. Furthermore, the deviation between the freezing kinetics was also observed when comparing the change in droplet volume. Initially, the rate of volume change was higher on the untreated surface compared to the superhydrophobic surface. However, at 25 % of the freezing time, the volume curves began to converge, indicating that the rate of volume change became larger on the FAS-10 surface.

4. Conclusions

A simple, low-cost, two-step process for fabricating superhydrophobic aluminum surfaces with enhanced corrosion and icing resistance is presented. The process consists of laser surface texturing followed by grafting using per-fluoroalkyl silane (FAS-10). The results of the topography measurements confirm that laser-texturing of Al was a crucial parameter in providing a micro/nano-pattern and aluminum oxide/hydroxide structure, which then acts as an active surface for further grafting with FAS-10. Laser-texturing and grafting for 1 h in FAS-10 solution resulted in a superhydrophobic aluminum surface with a water contact angle above 150°. SEM/EDS and XPS data confirmed that the FAS molecules evenly covered the aluminum surface and were covalently bonded on the aluminum surface (Al − O − Si bond). The superhydrophobic aluminum surface shows reduced wettability of the corrosion medium (dilute Harrison's solution). Due to trapped air in the formed structure, such treated surface shows excellent corrosion protection (enhanced passive behavior and up to 6 days of continuous durability). The low contact of a water droplet on the laser-textured+FAS-10 treated surface improved anti-icing performance through a significant delay of ice nucleation and extended freezing time. The fabricated aluminum surface is thus a great candidate for various applications necessitating corrosion and icing resistance through increased durability and functionality during exposure to the natural environment.

CRediT authorship contribution statement

Peter Rodič: Writing – original draft, Formal analysis, Conceptualization. **Nina Kovač:** Visualization, Methodology. **Slavko Kralj:** Writing – review & editing. **Samo Jereb:** Visualization, Methodology, Formal analysis. **Iztok Golobič:** Writing – review & editing, Supervision. **Matic Može:** Writing – original draft, Methodology, Formal analysis, Conceptualization. **Ingrid Milošev:** Writing – review & editing, Supervision.

Declaration of competing interest

The authors declare that they have no known competing financial interests or personal relationships that could have appeared to influence the work reported in this paper.

Data availability

Samples of the compounds are available from the authors.

Acknowledgements

The authors thank Prof. dr. Janez Kovač of the Department of Surface Engineering of the Jožef Stefan Institute for XPS measurements and Barbara Kapun, BSc, of the Department of Physical and Organic Chemistry of the Jožef Stefan Institute for SEM/EDS analyses. Center of Excellence in Nanoscience and Nanotechnology (CENN) is acknowledged for providing SEM/EDS analysis equipment.

Funding

The financial support from the Slovenian Research and Innovation Agency is acknowledged: research core funding No. P2-0393, P1-0134, P2-0089 and P2-0223; projects J2-50085, J2-3043, J2-3040, J2-3046, J3-3079 and J7-4420; bilateral projects BI-FR/23-24-PROTEUS-005 (PR-12039) and BI-RS/23-25-030 (PR-12782).

Appendix A. Supplementary data

Supplementary data to this article can be found online at https://doi.org/10.1016/j.surfcoat.2024.131325.

References

[1] J.E. Hatch, Aluminum: Properties and Physical Metallurgy, ASM International, 1984.
[2] J.B. Harrison, T.C.K. Tickle, Harrison solution, 1 Oil Color Chem 45, 1962, p. 571.
[3] A.M.A. Mohamed, A.M. Abdullah, N.A. Younan, Corrosion behavior of superhydrophobic surfaces: a review, Arab. J. Chem. 8 (2015) 749–765, https://doi.org/10.1016/j.arabjc.2014.03.006.
[4] E. Vazirinasab, R. Jafari, G. Momen, Application of superhydrophobic coatings as a corrosion barrier: a review, Surf. Coat. Technol. 341 (2018) 40–56, https://doi.org/10.1016/j.surfcoat.2017.11.053.
[5] D. Zhang, L. Wang, H. Qian, X. Li, Superhydrophobic surfaces for corrosion protection: a review of recent progresses and future directions, J. Coat. Technol. Res. 13 (2016) 11–29, https://doi.org/10.1007/s11998-015-9744-6.
[6] L. Cao, A.K. Jones, V.K. Sikka, J. Wu, D. Gao, Anti-icing superhydrophobic coatings, Langmuir 25 (2009) 12444–12448, https://doi.org/10.1021/la902882b.
[7] P. Rodič, I. Milošev, One-step ultrasound fabrication of corrosion resistant, self-cleaning and anti-icing coatings on aluminium, Surf. Coat. Technol. 369 (2019) 175–185, https://doi.org/10.1016/j.surfcoat.2019.03.082.
[8] P. Guo, Y. Zheng, M. Wen, C. Song, Y. Lin, L. Jiang, Icephobic/anti-icing properties of micro/nanostructured surfaces, Adv. Mater. 24 (2012) 2642–2648, https://doi.org/10.1002/adma.201104412.
[9] A.G. Nurioglu, A.C.C. Esteves, G. de With, Non-toxic, non-biocide-release antifouling coatings based on molecular structure design for marine applications, J. Mater. Chem. B 3 (2015) 6547–6570, https://doi.org/10.1039/C5TB00232J.
[10] F. Hizal, N. Rungraeng, J. Lee, S. Jun, H.J. Busscher, H.C. van der Mei, C.-H. Choi, Nanoengineered superhydrophobic surfaces of aluminum with extremely low bacterial adhesivity, ACS Appl. Mater. Interfaces 9 (2017) 12118–12129, https://doi.org/10.1021/acsami.7b01322.
[11] S.S. Latthe, A.B. Gurav, C.S. Maruti, R.S. Vhatkar, Recent progress in preparation of superhydrophobic surfaces: a review, J. Surf. Eng. Mater. Adv. Technol. 02 (2012) 76–94, https://doi.org/10.4236/jsemat.2012.22014.
[12] N.J. Shirtcliffe, G. McHale, S. Atherton, M.I. Newton, An introduction to superhydrophobicity, Adv. Colloid Interface Sci. 161 (2010) 124–138, https://doi.org/10.1016/j.cis.2009.11.001.
[13] Gh. Barati Darband, M. Aliofkhazraei, S. Khorsand, S. Sokhanvar, A. Kaboli, Science and engineering of superhydrophobic surfaces: review of corrosion resistance, chemical and mechanical stability, Arab. J. Chem. 13 (2020) 1763–1802, https://doi.org/10.1016/j.arabjc.2018.01.013.
[14] P. Rodič, B. Kapun, I. Milošev, Superhydrophobic aluminium surface to enhance corrosion resistance and obtain self-cleaning and anti-icing ability, Molecules 27 (2022) 1099, https://doi.org/10.3390/molecules27031099.
[15] R.V. Lakshmi, T. Bharathidasan, B.J. Basu, Superhydrophobic sol-gel nanocomposite coatings with enhanced hardness, Appl. Surf. Sci. 257 (2011) 10421–10426, https://doi.org/10.1016/j.apsusc.2011.06.122.
[16] Y. Zhang, J. Wu, X. Yu, H. Wu, Low-cost one-step fabrication of superhydrophobic surface on Al alloy, Appl. Surf. Sci. 257 (2011) 7928–7931, https://doi.org/10.1016/j.apsusc.2011.03.096.
[17] B. Zhang, Q. Zhu, Y. Li, B. Hou, Facile fluorine-free one step fabrication of superhydrophobic aluminum surface towards self-cleaning and marine

anticorrosion, Chem. Eng. J. 352 (2018) 625–633, https://doi.org/10.1016/j.cej.2018.07.074.
[18] C. Biloiu, I.A. Biloiu, Y. Sakai, Y. Suda, A. Ohta, Amorphous fluorocarbon polymer (a-C:F) films obtained by plasma enhanced chemical vapor deposition from perfluoro-octane (C8F18) vapor I: deposition, morphology, structural and chemical properties, J. Vac. Sci. Technol. A 22 (2003) 13–19, https://doi.org/10.1116/1.1624284.
[19] Y. Huang, D.K. Sarkar, X. Grant Chen, Superhydrophobic aluminum alloy surfaces prepared by chemical etching process and their corrosion resistance properties, Appl. Surf. Sci. 356 (2015) 1012–1024, https://doi.org/10.1016/j.apsusc.2015.08.166.
[20] I. Milošev, T. Bakarič, S. Zanna, A. Seyeux, P. Rodič, M. Poberžnik, F. Chiter, P. Cornette, D. Costa, A. Kokalj, P. Marcus, Electrochemical, surface-analytical, and computational DFT study of alkaline etched aluminum modified by carboxylic acids for corrosion protection and hydrophobicity, J. Electrochem. Soc. 166 (2019) C3131–C3146, https://doi.org/10.1149/2.0181911jes.
[21] P. Varshney, S.S. Mohapatra, A. Kumar, Superhydrophobic coatings for aluminium surfaces synthesized by chemical etching process, Int. J. Smart Nano Mater. 7 (2016) 248–264, https://doi.org/10.1080/19475411.2016.1272502.
[22] X. Yang, C. Yang, Z. Yang, D. Zhang, Corrosion resistance and stability of superhydrophobic surfaces with hierarchical micro/nanostructures induced by nanosecond and femtosecond lasers, Opt. Laser Technol. 169 (2024) 110179, https://doi.org/10.1016/j.optlastec.2023.110179.
[23] R. Parin, D.D. Col, S. Bortolin, A. Martucci, Dropwise condensation over superhydrophobic aluminium surfaces, J. Phys. Conf. Ser. 745 (2016) 1–8, https://doi.org/10.1088/1742-6596/745/3/032134.
[24] T. Nishino, M. Meguro, K. Nakamae, M. Matsushita, Y. Ueda, The lowest surface free energy based on $-CF_3$ alignment, Langmuir 15 (1999) 4321–4323, https://doi.org/10.1021/la981727s.
[25] M. Poberžnik, D. Costa, A. Hemeryck, A. Kokalj, Insight into the bonding of Silanols to oxidized aluminum surfaces, J. Phys. Chem. C 122 (2018) 9417–9431, https://doi.org/10.1021/acs.jpcc.7b12552.
[26] M. Poberžnik, A. Kokalj, Implausibility of bidentate bonding of the silanol headgroup to oxidized aluminum surfaces, Appl. Surf. Sci. 492 (2019) 909–918, https://doi.org/10.1016/j.apsusc.2019.04.032.
[27] J.-H. Kim, A. Mirzaei, H.W. Kim, S.S. Kim, Realization of superhydrophobic aluminum surfaces with novel micro-terrace nano-leaf hierarchical structure, Appl. Surf. Sci. 451 (2018) 207–217, https://doi.org/10.1016/j.apsusc.2018.04.187.
[28] I. Bernagozzi, C. Antonini, F. Villa, M. Marengo, Fabricating superhydrophobic aluminum: an optimized one-step wet synthesis using fluoroalkyl silane, Colloids Surf. A Physicochem. Eng. Asp. 441 (2014) 919–924, https://doi.org/10.1016/j.colsurfa.2013.05.042.
[29] J.-D. Brassard, D.K. Sarkar, J. Perron, Fluorine based superhydrophobic coatings, Appl. Sci. 2 (2012) 453–464, https://doi.org/10.3390/app2020453.
[30] N. Saleema, D.K. Sarkar, D. Gallant, R.W. Paynter, X.-G. Chen, Chemical nature of superhydrophobic aluminum alloy surfaces produced via a one-step process using fluoroalkyl-silane in a base medium, ACS Appl. Mater. Interfaces 3 (2011) 4775–4781, https://doi.org/10.1021/am201277x.
[31] W. Tong, D. Xiong, N. Wang, C. Yan, T. Tian, Green and timesaving fabrication of a superhydrophobic surface and its application to anti-icing, self-cleaning and oil-water separation, Surf. Coat. Technol. 352 (2018) 609–618, https://doi.org/10.1016/j.surfcoat.2018.08.035.
[32] A. Kumar, B. Gogoi, Development of durable self-cleaning superhydrophobic coatings for aluminium surfaces via chemical etching method, Tribol. Int. 122 (2018) 114–118, https://doi.org/10.1016/j.triboint.2018.02.032.
[33] P. Rodič, B. Kapun, M. Panjan, I. Milošev, Easy and fast fabrication of self-cleaning and anti-icing perfluoroalkyl silane film on aluminium, Coatings 10 (2020) 234, https://doi.org/10.3390/coatings10030234.
[34] M. Ruan, W. Li, B. Wang, B. Deng, F. Ma, Z. Yu, Preparation and anti-icing behavior of superhydrophobic surfaces on aluminum alloy substrates, Langmuir ACS J. Surf. Colloids 29 (2013) 8482–8491, https://doi.org/10.1021/la400979d.
[35] N. Sharifi, A. Dolatabadi, M. Pugh, C. Moreau, Anti-icing performance and durability of suspension plasma sprayed TiO2 coatings, Cold Reg. Sci. Technol. 159 (2019) 1–12, https://doi.org/10.1016/j.coldregions.2018.11.018.
[36] Z. Liu, F. Zhang, Y. Chen, H. Zhang, Y. Han, J. Liu, L. Huang, X. Liu, Electrochemical fabrication of superhydrophobic passive films on aeronautic steel surface, Colloids Surf. A Physicochem. Eng. Asp. 572 (2019) 317–325, https://doi.org/10.1016/j.colsurfa.2019.04.033.
[37] B. Bhushan, E.K. Her, Fabrication of superhydrophobic surfaces with high and low adhesion inspired from rose petal, Langmuir 26 (2010) 8207–8217, https://doi.org/10.1021/la904585j.
[38] L. Wang, Q. Gong, S. Zhan, L. Jiang, Y. Zheng, Robust anti-icing performance of a flexible superhydrophobic surface, Adv. Mater. 28 (2016) 7729–7735, https://doi.org/10.1002/adma.201602480.
[39] Y. Du, L. Hu, L. Dong, S. Du, D. Xu, Experimental study on anti-icing of robust TiO2/Polyurea superhydrophobic coating, Coatings 13 (2023) 1162, https://doi.org/10.3390/coatings13071162.
[40] W. Hou, Y. Shen, J. Tao, Y. Xu, J. Jiang, H. Chen, Z. Jia, Anti-icing performance of the superhydrophobic surface with micro-cubic array structures fabricated by plasma etching, Colloids Surf. A Physicochem. Eng. Asp. 586 (2020) 124180, https://doi.org/10.1016/j.colsurfa.2019.124180.
[41] Y. Lu, Temperature dependent anti-icing performance of the microstructure surface: wettability change and ice nucleation, Coatings 13 (2023) 1485, https://doi.org/10.3390/coatings13091485.
[42] S. Li, M. Zhong, Y. Zou, M. Xu, X. Liu, X. Xing, H. Zhang, Y. Jiang, C. Qiu, W. Qin, M. Li, Q. He, C. Zhou, Fabrication of micron-structured heatable graphene hydrophobic surfaces for deicing and anti-icing by laser direct writing, Coatings 13 (2023) 1559, https://doi.org/10.3390/coatings13091559.
[43] W. Xing, Z. Li, H. Yang, X. Li, X. Wang, N. Li, Anti-icing aluminum alloy surface with multi-level micro-nano textures constructed by picosecond laser, Mater. Des. 183 (2019) 108156, https://doi.org/10.1016/j.matdes.2019.108156.
[44] H. Wang, M. He, H. Liu, Y. Guan, One-step fabrication of robust superhydrophobic steel surfaces with mechanical durability, thermal stability, and anti-icing function, ACS Appl. Mater. Interfaces 11 (2019) 25586–25594, https://doi.org/10.1021/acsami.9b06865.
[45] A. Volpe, C. Gaudiuso, L. Di Venere, F. Licciulli, F. Giordano, A. Ancona, Direct femtosecond laser fabrication of superhydrophobic aluminum alloy surfaces with anti-icing properties, Coatings 10 (2020) 587, https://doi.org/10.3390/coatings10060587.
[46] Y.L. Zhan, M. Ruan, W. Li, H. Li, L.Y. Hu, F.M. Ma, Z.L. Yu, W. Feng, Fabrication of anisotropic PTFE superhydrophobic surfaces using laser microprocessing and their self-cleaning and anti-icing behavior, Colloids Surf. A Physicochem. Eng. Asp. 535 (2017) 8–15, https://doi.org/10.1016/j.colsurfa.2017.09.018.
[47] D.P. Subedi, Contact angle measurement for the surface characterization of solids, Himal. Phys. 2 (2011) 1–4, https://doi.org/10.3126/hj.v2i2.5201.
[48] F. Boulogne, A. Salonen, Drop freezing: fine detection of contaminants by measuring the tip angle, Appl. Phys. Lett. 116 (2020) 103701, https://doi.org/10.1063/1.5144071.
[49] Y. Shang, B. Bai, Y. Hou, X. Zhong, L. Sun, Alteration of freezing paradigms of an impact water droplet on different cold surfaces, Int. J. Heat Mass Transf. 183 (2022) 122177, https://doi.org/10.1016/j.ijheatmasstransfer.2021.122177.
[50] F. Chu, X. Zhang, S. Li, H. Jin, J. Zhang, X. Wu, D. Wen, Bubble formation in freezing droplets, Phys. Rev. Fluids 4 (2019) 071601, https://doi.org/10.1103/PhysRevFluids.4.071601.
[51] J.E. Castillo, Y. Huang, Z. Pan, J.A. Weibel, Asymmetric solidification during droplet freezing in the presence of a neighboring droplet, Int. J. Heat Mass Transf. 171 (2021) 121134, https://doi.org/10.1016/j.ijheatmasstransfer.2021.121134.
[52] NIST X-ray Photoelectron Spectroscopy Database, NIST Stand. Ref. Database Number 20, National Institute of Standards and Technology, Gaithersburg MD, 2000. https://srdata.nist.gov/xps/Default.aspx.
[53] M. Poberžnik, Quantum Mechanical Modeling of the Oxidation of Aluminum Surfaces and their Interactions with Corrosion Inhibitors, Doctoral thesis,, University of Ljubljana, Ljubljana, Slovenia, 2019, pp. 75–83.
[54] W.M. Steen, J. Mazumder, Laser surface treatment, in: W.M. Steen, J. Mazumder (Eds.), Laser Mater. Process, Springer, London, 2010, pp. 295–347, https://doi.org/10.1007/978-1-84996-062-5_7.
[55] J. Long, M. Zhong, H. Zhang, P. Fan, Superhydrophilicity to superhydrophobicity transition of picosecond laser microstructured aluminum in ambient air, J. Colloid Interface Sci. 441 (2015) 1–9, https://doi.org/10.1016/j.jcis.2014.11.015.
[56] P.L.J. Gunter, O.L.J. Gijzeman, J.W. Niemantsverdriet, Surface roughness effects in quantitative XPS: magic angle for determining overlayer thickness, Appl. Surf. Sci. 115 (1997) 342–346, https://doi.org/10.1016/S0169-4332(97)00007-X.
[57] I. Milošev, Ž. Jovanović, J.B. Bajat, R. Jančić-Heinemann, V.B. Mišković-Stanković, Surface analysis and electrochemical behavior of aluminum pretreated by Vinyltriethoxysilane films in mild NaCl solution, J. Electrochem. Soc. 159 (2012) C303–C311, https://doi.org/10.1149/2.042207jes.
[58] J.B. Bajat, I. Milošev, Ž. Jovanović, R.M. Jančić-Heinemann, M. Dimitrijević, V. B. Mišković-Stanković, Corrosion protection of aluminium pretreated by vinyltriethoxysilane in sodium chloride solution, Corros. Sci. 52 (2010) 1060–1069, https://doi.org/10.1016/j.corsci.2009.11.035.
[59] H. Sugimura, K. Ushiyama, A. Hozumi, O. Takai, Lateral force on fluoroalkylsilane self-assembled monolayers dependent on molecular ordering, J. Vac. Sci. Technol. B Microelectron. Nanometer Struct. Process. Meas. Phenom. 20 (2002) 393–395, https://doi.org/10.1116/1.1431955.
[60] D.N.G. Krishna, J. Philip, Review on surface-characterization applications of X-ray photoelectron spectroscopy (XPS): recent developments and challenges, Appl. Surf. Sci. Adv. 12 (2022) 100332, https://doi.org/10.1016/j.apsadv.2022.100332.
[61] I. Balchev, N. Minkovski, Ts. Marinova, M. Shipochka, N. Sabotinov, Composition and structure characterization of aluminum after laser ablation, Mater. Sci. Eng. B 135 (2006) 108–112, https://doi.org/10.1016/j.mseb.2006.08.042.
[62] R. Jagdheesh, M. Diaz, J.L. Ocaña, Bio inspired self-cleaning ultrahydrophobic aluminium surface by laser processing, RSC Adv. 6 (2016) 72933–72941, https://doi.org/10.1039/C6RA12236A.
[63] L.B. Boinovich, A.M. Emelyanenko, A.D. Modestov, A.G. Domantovsky, K. A. Emelyanenko, Synergistic effect of superhydrophobicity and oxidized layers on corrosion resistance of aluminum alloy surface textured by nanosecond laser treatment, ACS Appl. Mater. Interfaces 7 (2015) 19500–19508, https://doi.org/10.1021/acsami.5b06217.
[64] G. Yoganandan, T. Bharathidasan, M. Soumya Sri, D. Vasumathy, J.N. Balaraju, B. J. Basu, Effect of anodized oxide layer aging on wettability of alkyl silane coating developed on aerospace aluminum alloy, Metall. Mater. Trans. A 46 (2015) 337–346, https://doi.org/10.1007/s11661-014-2627-0.
[65] P. Rodič, I. Milošev, M. Lekka, F. Andreatta, L. Fedrizzi, Corrosion behaviour and chemical stability of transparent hybrid sol-gel coatings deposited on aluminium in acidic and alkaline solutions, Prog. Org. Coat. 124 (2018) 286–295, https://doi.org/10.1016/j.porgcoat.2018.02.025.
[66] T. Liu, S. Chen, S. Cheng, J. Tian, X. Chang, Y. Yin, Corrosion behavior of superhydrophobic surface on copper in seawater, Electrochim. Acta 52 (2007) 8003–8007, https://doi.org/10.1016/j.electacta.2007.06.072.
[67] F.J. Martin, G.T. Cheek, W.E. O'Grady, P.M. Natishan, Impedance studies of the passive film on aluminium, Corros. Sci. 47 (2005) 3187–3201, https://doi.org/10.1016/j.corsci.2005.05.058.

[68] F. Mansfeld, S. Lin, S. Kim, H. Shih, Electrochemical impedance spectroscopy as a monitoring tool for passivation and localized corrosion of aluminum alloys, Mater. Corros. 39 (1988) 487–492, https://doi.org/10.1002/maco.19880391102.
[69] N. Maeda, Brief overview of ice nucleation, Molecules 26 (2021) 392, https://doi.org/10.3390/molecules26020392.
[70] A.G. Marín, O.R. Enríquez, P. Brunet, P. Colinet, J.H. Snoeijer, Universality of tip singularity formation in freezing water drops, Phys. Rev. Lett. 113 (2014) 054301, https://doi.org/10.1103/PhysRevLett.113.054301.
[71] X. Zhang, X. Wu, J. Min, X. Liu, Modelling of sessile water droplet shape evolution during freezing with consideration of supercooling effect, Appl. Therm. Eng. 125 (2017) 644–651, https://doi.org/10.1016/j.applthermaleng.2017.07.017.
[72] M. Tembely, A. Dolatabadi, A comprehensive model for predicting droplet freezing features on a cold substrate, J. Fluid Mech. 859 (2019) 566–585, https://doi.org/10.1017/jfm.2018.839.
[73] S. Akhtar, M. Xu, M. Mohit, A.P. Sasmito, A comprehensive review of modeling water solidification for droplet freezing applications, Renew. Sustain. Energy Rev. 188 (2023) 113768, https://doi.org/10.1016/j.rser.2023.113768.
[74] C. Guo, D. Maynes, J. Crockett, D. Zhao, Heat transfer to bouncing droplets on superhydrophobic surfaces, Int. J. Heat Mass Transf. 137 (2019) 857–867, https://doi.org/10.1016/j.ijheatmasstransfer.2019.03.103.